

Nickel Hexacyanoferrate Electrodes for Cation Intercalation Desalination

Slawomir Porada,¹ Pamela Bukowska,¹ A. Shrivastava,² P.M. Biesheuvel,¹ and Kyle C. Smith^{3,4,5,*}

¹Wetsus, European Centre of Excellence for Sustainable Water Technology, Oostergoweg 9, 8911 MA Leeuwarden, The Netherlands. ²Department of Materials Science and Engineering, University of Illinois at Urbana-Champaign, Urbana, IL 61801. ³Department of Mechanical Science and Engineering, University of Illinois at Urbana-Champaign, Urbana, IL 61801. ⁴Computational Science and Engineering Program, University of Illinois at Urbana-Champaign, Urbana, IL 61801. ⁵Beckman Institute, University of Illinois at Urbana-Champaign, Urbana, IL 61801. *Corresponding author's email: kcsmith@illinois.edu

Abstract

Using porous electrodes containing redox-active nickel hexacyanoferrate (NiHCF) nanoparticles, we construct and test a device for electrochemical water desalination in a two flow-channel device where the electrodes are in direct contact with an anion-exchange membrane. Upon reduction of NiHCF, cations intercalate into it and the water in its vicinity is desalinated; at the same time water in the opposing electrode becomes more saline upon oxidation of NiHCF in that electrode. In a cyclic process of charge and discharge, fresh water is continuously produced, alternating between the two channels in sync with the direction of applied current. Compared to capacitive deionization using porous carbon electrodes, a higher salt adsorption capacity per cycle is achieved, much lower cell voltages are needed, and the energy costs of desalination can be significantly reduced.

Electrochemical water desalination with porous electrodes can make use of two fundamentally different mechanisms for salt storage. The first mechanism is capacitive electrosorption, where ions are held in electrical double layers (EDLs) formed in the micropores of porous electrodes comprised of ideally polarizable material (e.g., carbon) [1]. In the second mechanism, which has recently begun research exploration [2–6], intercalation electrodes are used where ions are stored within the sites of a solid-state host compound.

The first mechanism, capacitive electrosorption, is used in Capacitive Deionization (CDI), a process in which ions are held near the carbon surface in the diffuse part of the EDL. CDI electrodes are made of carbon (carbon nanotubes, graphene, activated carbon powder, etc.) which can be processed into porous, ion- and electron-conducting, thin electrode films, suspensions, or fluidized beds [7]. CDI based on capacitive EDL charging is a promising method, but to reach a certain salt adsorption capacity (SAC; a typical number being of the order of SAC=5–15 mg/g, referring to mass of NaCl removed, per total mass of carbon in a two-electrode cell, measured at a standard cell voltage of $V_{cell}=1.2$ V), the energy input is not insignificant [8–10], while the current

efficiency λ (quantifying the fraction of current input that results in salt adsorption) of CDI cells can be well below unity, implying that in the charging process not only counterions adsorb but also coions desorb from the electrode [11]. In CDI with membranes, or using improved charging schemes, λ can be close to unity [10].

Like capacitive carbons, intercalation host compounds (IHCs) can be incorporated into porous electrode films and can adsorb charge, but the ion storage mechanism of IHCs is fundamentally different from EDL charging. In intercalation electrodes, ions are stored in the crystallographic sites of the IHC as a result of its redox activity. Water desalination using IHCs, which is currently much less developed and utilized than CDI, has the advantage that to reach a certain SAC a much lower voltage and energy is needed than using capacitive electrosorption, because the change in electrode potential with electrode charge can be much lower. Also, IHCs have the potential to selectively remove one ion (e.g., Na^+) out of a multi-ion mixture with other ions of the same valence and charge.

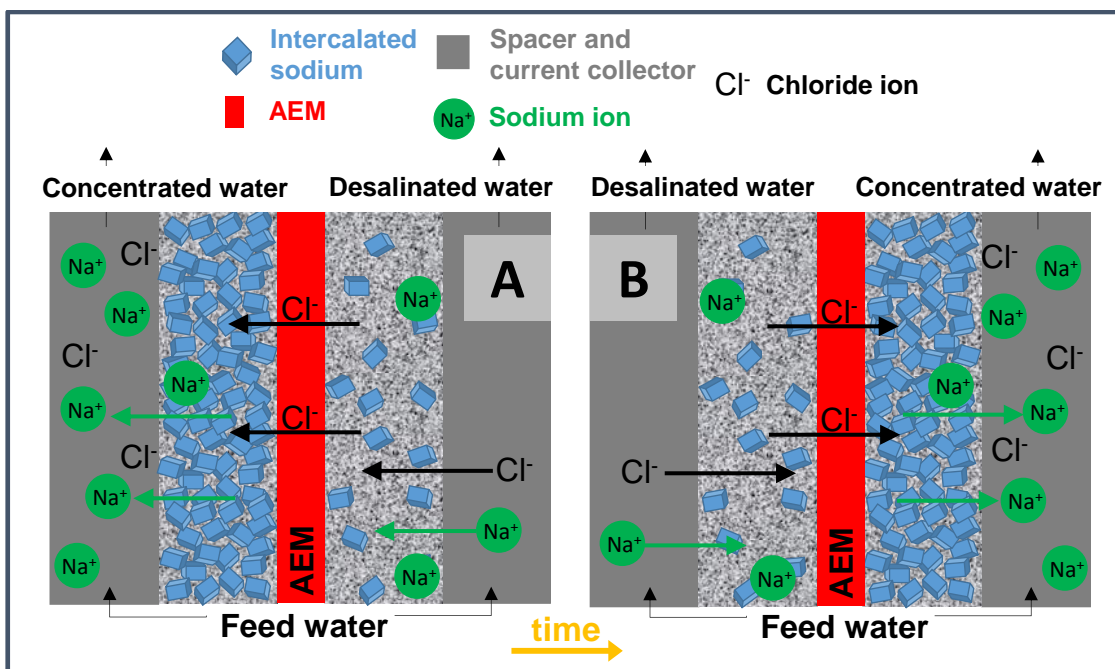


Figure 1. Schematic diagram of the present CID flow cell with a single anion exchange membrane (AEM) and two adjacent and identical electrodes containing NiHCF IHC. A flow channel (“spacer”) is attached to each current collector and two of these structures sandwich the cell. In one half of the cycle (A), sodium ions de-intercalate from the left IHC while chloride ions migrate through the membrane, to the left, producing water of increased salinity on the left-hand side. During this stage, electronic current runs to this electrode through the external circuit. At the same time, on the right-hand side, sodium ions intercalate into the PBA, and desalinated water is produced. After some time, the maximum amount of intercalated sodium is reached in the right-hand electrode and the current direction must be reversed (panel B).

The use of IHCs for water desalination has been reported using several novel cell architectures. The “Desalination Battery,” a cell consisting of one $\text{Na}_2\text{Mn}_5\text{O}_{10}$ (NMO) electrode and one Ag/AgCl electrode, was used for water desalination by adsorption of cations within NMO and adsorption of Cl^- ions by conversion of Ag to AgCl [3]. In “Hybrid CDI” [2], an IHC electrode (either NMO [2] or $\text{Na}_2\text{FeP}_2\text{O}_7$ [12]) was combined with a carbon capacitive electrode for anion adsorption. In both of these desalination devices a single cation-intercalating electrode was paired with a different electrode that adsorbs anions. Later, Smith and Dmello (SD) [4,13] proposed desalination with Na-ion IHC electrodes having identical chemical composition, originally referred to as “Na-Ion Desalination (NID)” [4]. Presently, we refer to this technology as Cation Intercalation Desalination (CID) to emphasize the charge adsorption mechanism by which desalination is achieved. While the use of the same IHC in both electrodes is impractical for battery use, SD showed that desalination is possible, in theory, with electrodes of identical composition. To achieve this, an innovative cell design was proposed where porous IHC electrode films are placed on either side of a separator layer with feed water in a “flow-through” mode directed through the electrode, along the separator layer. SD showed that for an IHC that is cation-adsorbing, the separator layer must be cation-blocking to achieve high salt removal, i.e., an anion-exchange membrane (AEM) must be used. In this way a CID device operates where, during one half of a charging-discharging cycle, one channel produces desalinated water and the other brine, and, during the other half of the cycle, the situation is reversed. Recently, Srimuk *et al.* experimentally demonstrate the use of identical intercalation electrodes for desalination in a membraneless cell, where a MXene intercalation compound is used which is host to both anions and cations. Xing *et al.* recently used a hybrid cell with MoS_2 as a cathode, combined with a capacitive anode [6].

The recent development of IHCs for aqueous rechargeable Na-ion batteries (ARSBs) has been stimulated by the low cost compared with non-aqueous Li-ion systems and by the inherent safety of water-based electrolytes [14]. By leveraging the CID device concept these developments can be applied to electrochemical water desalination. Also, the plethora of Na-ion IHCs developed as cathodes for ARSBs can be applied as both cathode and anode in CID, eliminating the need to search for low-potential IHCs, which, for ARSBs, are less numerous compared to high-potential IHCs. Theoretical predictions of CID performance were originally obtained [4] using symmetric cells with either NMO, a common ASRB cathode [15–17], or $\text{NaTi}_2(\text{PO}_4)_3$ (NTP), a common ASRB anode [16,18,19]. These respective materials have high specific capacities of 45 mAh/g-NMO [15] and 120 mAh/g-NTP [16], but other IHCs exist that also show promise for use in CID. Among the various cathode compounds developed, nanoparticulate Prussian Blue Analogues (PBAs) stand apart for their high cycle life and facile cation intercalation kinetics that have enabled their demonstration use in Na^+ [20–23], K^+ [20,21], Mg^{2+} [24], Ca^{2+} [24,25], and Zn^{2+} [26] ion batteries. Here, we use a particular PBA, nickel hexacyanoferrate (NiHCF), to exchange Na ions reversibly with saline

solution flowing through a CID cell. Its average reduction potential of ~0.6 V vs. SHE [20,23], though modest as a cathode in ARSBs, is 200 mV below the O₂ evolution potential at neutral pH. As a result, minimal electrolyte decomposition is expected even at large overpotentials applied to CID cells using these IHCs. Also, Smith recently predicted that NiHCF has sufficient capacity to desalinate seawater [27]. Based on the results in our present work, we calculate that this material can potentially achieve in brackish water SACs of ~40 mg/g-electrode (assuming 59 mAh/g-NiHCF capacity [20,23]; current efficiency 92%; charge capacity utilization 85%; IHC 80 wt% of electrode mass; parameters to be explained later on).

In this work we test and demonstrate desalination within a CID cell for the first time experimentally. Here, desalination is achieved by using redox-active NiHCF nanoparticles to intercalate Na⁺ ions from NaCl solution. We synthesize Na-rich NiHCF using precipitation chemistry and fabricate porous electrode films from them. Prior to CID cell testing electrochemical titration is used to characterize the equilibrium relationship between potential and stored charge in a half-cell using non-flowing, concentrated Na₂SO₄ electrolyte. These porous electrode films are then integrated within a CID cell adjacent to an AEM (Fig. 1). Feed water is flowed behind the porous electrodes through flow channels adjoined to each of the cell's current collectors, enabling continuous desalination of feed water. The dynamic, cyclic operation of this CID cell is subsequently characterized at a salinity that is representative of brackish water. A systematic study of desalination performance is then conducted by varying cycle time with the same current in each case, demonstrating the range of electrode charge, salt adsorption capacity, and energy consumption achievable using NiHCF nanoparticles in a CID cell.

NiHCF has previously been synthesized for Na-ion batteries in both Na-deficient [20] and Na-rich [23] forms, the latter form enabling batteries to be assembled and charged without pre-sodiation when it is used as a positive electrode. In this work, we synthesize NiHCF in a Na-rich state, with Na₂NiFe(CN)₆ being the ideal composition [19]. Synthesis of Na-rich NiHCF (with Na₄Fe(CN)₆ precursor) eliminates introduction of additional cationic species that are present in the typical synthesis of Na-deficient NiHCF, which, for example, used K₃Fe(CN)₆ precursor in ref. [20] and, thus, resulted in K⁺ within the synthesized NiHCF structure. The present Na-rich NiHCF material is later converted to intermediate compositions via electrochemical oxidation in a three-electrode cell. NiHCF particles undergo nucleation and growth as the precursors are combined, and the manner in which this is done will affect the final particle size distribution as well as the crystallinity of the synthesized particles. We use a solution/precipitation method with consistent reaction conditions to synthesize NiHCF (see Methods).

Based on ex situ elemental analysis Na-rich (as-prepared) NiHCF samples were found to have a composition of Na_{1.20}Ni_{1.28}Fe_{1.22}C₆N_{5.75}·4.41H₂O (see Methods). This composition includes

significantly less Na per formula unit CN than that of the theoretical composition ($\text{Na}_2\text{NiFe}(\text{CN})_6$), also with a substantial amount of hydrated H_2O within its lattice. In light of these factors, the presence of H_2O trapped within the interstitial sites of the NiHCF structure may play a role in limiting the incorporation of Na^+ ions. Despite their non-ideal composition, we note that the present NiHCF possesses more than double the degree of alkali cation intercalation and similar nickel stoichiometry per CN formula unit compared with those of Na/K-deficient NiHCF synthesis ($\text{K}_{0.6}\text{Ni}_{1.2}\text{Fe}(\text{CN})_6 \cdot 3.6\text{H}_2\text{O}$, ref. [20]). These observations demonstrate that we have successfully synthesized Na-rich NiHCF. The crystal structure of as-synthesized NiHCF was confirmed by X-ray diffraction (see Methods) to belong to the $\text{Fm}3\text{m}$ space group with a lattice parameter of 10.25 Å, in good agreement with literature [20]. Peak positions match well with previous reports in literature for Prussian Blue [28] and NiHCF [20,23] (see Supplementary Information, SI). The crystallinity and physical morphology of NiHCF particles were analyzed using transmission (TEM) and scanning electron microscopy (SEM, see SI). TEM images show nanocrystallites between 2 to 7 nm, with mean crystallite size of approximately 4 nm. Nanocrystallite shapes appear as rounded cubes (in contrast with previous reports of highly faceted PBA nanoparticles [29]), likely as a result of crystal defects introduced during nanocrystal growth. SEM images of the NiHCF particles showed a range of primary and secondary particle sizes. While secondary particles were observed with diameters on the order of 10 µm, detailed examination at higher magnification reveals the presence of nanoparticles with diameters on the order of 100 nm, consistent with prior reports on NiHCF [20,23].

The nanoparticulate morphology of NiHCF was further corroborated by N_2 gas adsorption measurements. This measurement was also used to assess the size distribution of pores within the electrodes (see Methods). As shown in the SI, in the range up to 30 nm pore size, porosity analysis of synthesized NiHCF powder resulted in a pore volume of 0.028 mL/g, a BET area of 15 m^2/g , and a surface area using non-linear NLDFT theory of 12 m^2/g [30]. Assuming a density for NiHCF of 2.0 g/mL (based on its ideal stoichiometry and XRD analysis), we find a corresponding pore volume per unit NiHCF volume of 5.6%, revealing ultra-low microporosity indicative of nanoparticle aggregation. Accordingly, this powder was ball milled to separate nanoparticle aggregates (see Methods). Electrodes were subsequently prepared using a procedure similar to that reported in ref. [31], combining 80 wt% NiHCF with 10 wt% PTFE binder and 10 wt% conductive carbon black, after which the electrodes were calendered to increase electronic conductivity (see Methods). After this process the BET area of the electrode was 103 m^2/g , and pore volume (in the range to 30 nm pore size) was 0.12 mL/g or 29 vol% (assuming 2.0 g/mL density, as before), confirming the separation of nanoparticulate aggregates that is necessary for high electrochemical activity. SEM characterization of the electrode showed a homogeneous microstructure consisting of NiHCF, carbon black, and macroporosity (see SI). The macropores within the electrode (which, during cell operation, is filled with saline water) are estimated to have a porosity of 40 to 50 vol%.

In the context of desalination by CID, electrode charge translates to salt removal, as Na ions are the primary intercalant species storing charge within the electrodes, and, therefore, understanding the cycling characteristics of each electrode is essential to constructing a high-performance CID cell. To illustrate this principle, consider a dimensionless number between 0 and 1 denoting the fraction of cation-filled sites within the IHC, hereafter referred to as the intercalation degree θ . For an electrode with $\theta=0$ the IHC contains no exchangeable intercalant, while at $\theta=1$ the IHC is saturated with intercalant. To convert from intercalation degree θ , for which $0 < \theta < 1$, to electrode charge Q in mAh/g, we multiply by the maximum charge Q_{\max} at full intercalation, i.e., $Q=Q_{\max}\theta$. For the half-cell cycling results discussed later, equivalent spans of these two scales are shown in Fig. 2B. In desalination with Na-ion IHCs (such as NiHCF), the intercalation degree within opposing electrodes evolves (on average) in a symmetrical fashion when side reactions are negligible, switching in the fraction of intercalated Na, θ , between two states of θ (see ref. [4,32]). During one half of the cycle the composition in one electrode changes from θ_1 to θ_2 ($\theta_2 > \theta_1$), while in the other electrode, simultaneously, the composition changes from θ_4 to θ_3 ($\theta_4 > \theta_3$). Such operation is referred to as the “rocking-chair” cycling mechanism utilized commonly in Li-ion [33] and many other rechargeable batteries using IHCs. The importance of this principle to the CID concept is exactly this: cations are intercalated from the electrolyte in one electrode, while at identical rate cations are deintercalated into the electrolyte in the opposing electrode [4]. When the IHCs in both electrodes are identical and are of equal mass, this action produces an equal and opposite change in composition, i.e., $\theta_2-\theta_1=\theta_4-\theta_3$. Thus, based on the use of IHCs an innovative cell design is proposed with only one ion-exchange membrane and two chemically identical IHC electrodes.

Half-cells of NiHCF electrodes were characterized in 1 M Na_2SO_4 solution (often used in ARSBs) using the galvanostatic intermittent titration technique (GITT, see Methods). Typically, when IHCs are used for energy storage in batteries, the principal metric of consideration is the maximum electrode charge in mAh/g. The equilibrium potential versus electrode charge in Fig. 2B, extracted from GITT, shows a maximum charge of 59 mAh/g (similar to previous reports for NiHCF [20,23]) with a region in which potential varies in a roughly linear manner between 5 and 55 mAh/g (per gram NiHCF in one electrode). From half-cell characterization we also find that the relationship between equilibrium potential and the intercalation degree within NiHCF particles can be correlated by the Temkin isotherm [37],

$$E=E_{\text{ref}}-RT/F^*\ln(c_{\text{Na},\infty}/c_0 \cdot \theta/(1-\theta))-g\cdot\theta, \quad (1)$$

where at room temperature $RT/F=25.6$ mV and the interaction parameter g is positive when intercalated Na-ions in the IHC repel one another, and therefore do not phase-separate into Na-rich and Na-deficient regions (which is predicted when $g < -100$ mV). Here, $c_{\text{Na},\infty}$ is the Na^+ concentration within the electrolyte surrounding IHC particles, and $c_0=1$ M is a reference concentration. A best fit

to the data is obtained using $E_{\text{ref}}=510$ mV vs. Ag/AgCl and $g=+90$ mV. Such a correlation is also an essential input for porous-electrode modeling of Na-ion batteries and CID, which can affect the dynamic of ions within electrodes during operation [4,38].

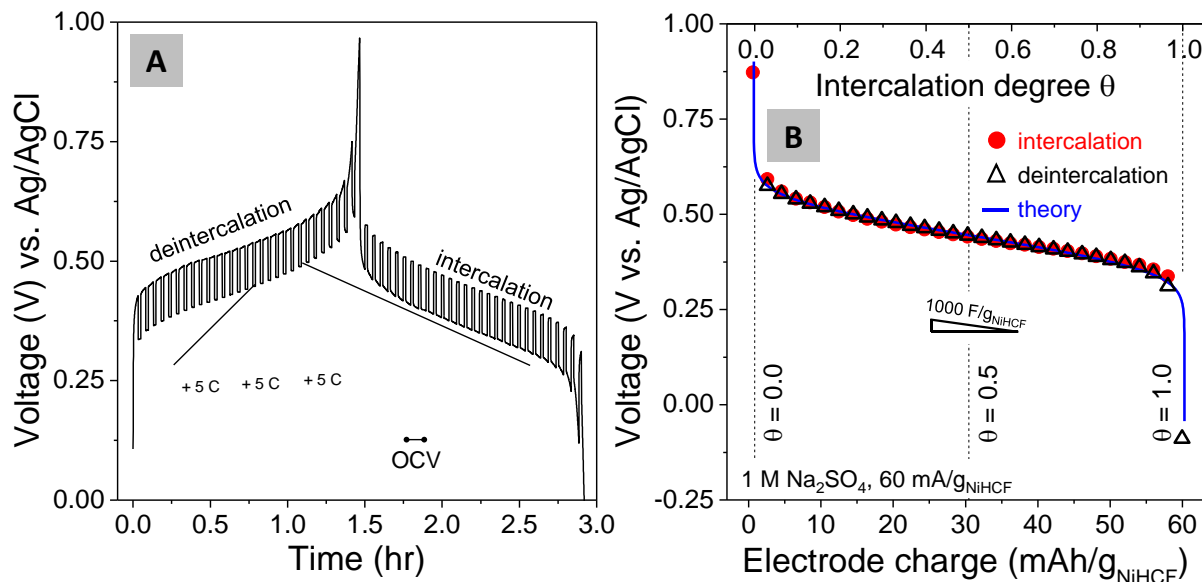


Figure 2. Electrochemical titration of a single NiHCF IHC in 1 M Na_2SO_4 . In this experiment, a constant current of 60 mA/g of NiHCF is applied for 118 s, after which current is set to zero for 60 s. Around 1.5 hr, current direction is reversed. From the time-dependent trace of voltage (panel A), we take the voltage at the end of the “rest”-period and construct panel B, which shows the equilibrium potential vs charge of the NiHCF-material, with excellent reversibility between de- and intercalation of Na^+ . The Temkin-equation fits data according to Eq. (1) well.

To compare CID performance for the present electrodes to that of typical capacitive electrodes in CDI, we calculated the differential capacitance, $-\text{d}Q/\text{d}E$. Over the linear range of potential variation, capacitance exceeds 1000 F/g, which is much higher than values for purely capacitive electrodes which are typically not higher than 100 F/g defined per single electrode voltage and single electrode mass. This difference in capacitance implies that, to store the same charge, a much lower voltage is needed for intercalation electrodes than for capacitive electrodes. As an example, to achieve the same salt adsorption capacity, with C ten-fold higher (as for IHC electrodes compared to capacitive ones) and assuming the same current efficiency, we require a final cell voltage that is ten-fold lower, and thus, with the energy proportional to $C \cdot V^2$, the energy input can be ten-fold lower.

Desalination experiments, as reported in Fig. 3, are performed at a salt concentration in the feed water of 20 mM and a current density of 2.8 A/m² (see Methods). A constant current (CC) mode was used because (1) simulation has predicted that such operation produces nearly constant effluent concentration after an initial transient period [4,39] and (2) recent analysis of CDI cycling modes has shown that the CC mode is more energy efficient than the constant potential mode [9]. This particular current density is small in comparison with typical CDI experiments, but large cell

polarization at high currents prevented further increases in current density at the present feed water salinity level. The large cell voltages that developed at higher currents may be due to an ion transport rate limitation in the cell. Specifically, Na^+ ions must transport between the porous electrode and the flow channel, and Cl^- ions must transport between the porous electrodes on opposing sides of the cell through the membrane. Thus, the microstructure and thickness of the porous electrodes, as well as those of the flow channels, can be optimized to enable efficient operation at higher rates, as has been predicted previously [4]. In addition, because NiHCF is a type of metal-organic framework whose CN^- ligands are poorly conducting, electronic conduction is expected to be slow within these particles. As such, it is possible that the inhomogeneous distribution of conductive carbon black could limit the transmission of electrons to NiHCF particles. Solid-state diffusion of Na^+ ions within NiHCF particles may also have played a role, depending on the degree of size dispersity among them. Membrane resistance is not expected to affect performance substantially due to the high concentration of membrane fixed charge in comparison with influent salinity. The exact reason for the high resistance remains to be identified and solved.

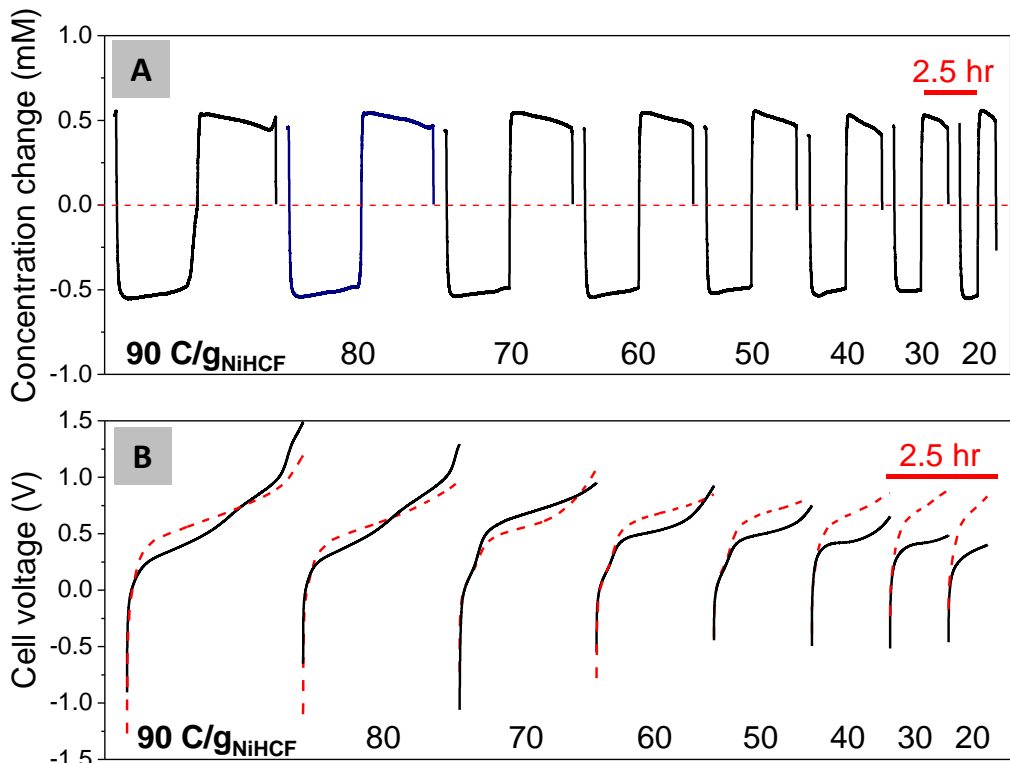


Figure 3. Desalination cycles using NiHCF IHCs at a constant current of 2.8 A/m^2 in 20 mM NaCl , for sets of cycles where the charging time is reduced after each 2 or 3 cycles, starting at a situation where one electrode is almost completely intercalated with Na^+ , and the other is in an almost completely deintercalated state. Panel A presents one cycle from each set of 2 or 3 similar cycles, showing both desalination (concentration change < 0) and salt release (concentration change > 0). Note that here only results for the effluent salinity from one of the two channels is shown. In panel B profiles of cell voltage versus time are shown during the same desalination cycle. Here, to show the symmetry in the process, the voltage trace during the second half of the cycle is vertically switched and moved left, to overlap with the voltage trace in the earlier half-cycle.

To characterize desalination dynamics, we measure the time variation of effluent salinity and cell voltage in cycles of different duration but at the same current. Data in Fig. 3 were obtained in cell where initially one electrode is almost completely de-intercalated and the other almost fully intercalated following the approach proposed by SD [4]. Here, the total charge transferred between electrodes was reduced from 90 to 20 C/g-NiHCF in steps of 10 C/g every 2-3 cycles (Fig 3 shows results of one cycle for each condition). In the SI we present results of a different experiment where the cell starts with two electrodes that initially have a similar intercalation degree θ (in the range 0.4-0.6). Here, the total charge transferred during each cycle was varied in a similar manner to that of the first routine, but in increasing order from 20 to 90 C/g-NiHCF. Results of this experiment match very closely with those presented in Fig. 3. In Fig. 3, panel A shows the effluent salinity (minus inflow salinity) during one cycle, as measured in the effluent of one of the two channels. It is expected that the other channel has exactly opposite (“symmetric”) behavior, i.e., a salinity-versus-time trace that is the mirror image (reflection about the horizontal dashed line) of the one measured. This expectation is based on the fact that both channels and electrodes are chemically identical (except for the fact that at any moment in time the value of θ will be different), and that voltage-versus-time traces during charging and discharging overlap quite well, as shown in panel B. Thus, though we did not measure the salt effluent salinity from both channels simultaneously, it is difficult to envision a scenario where one channel exhibits the behavior presented in Fig. 3, while the effluent salinity-versus-time trace in the opposing channel would be very different. Nevertheless, in future work it is relevant to measure the effluent salinity of both channels simultaneously.

In Fig. 3, panel A shows that effluent salinity change (i.e., the difference between effluent and inlet salinity levels) is fairly constant, in line with the expectation for operation at constant current. With decreasing charge transfer, the half-cycle time of charging and discharging (desalination and salt release) decreases, from around 5 hr in the longest experiments (i.e., for a charge of 90 C/g, defined per unit NiHCF mass in both electrodes) to 1 hr at 20 C/g-NiHCF, but for all cycles the influent/effluent salinity change is constant. The cell voltage during charge and discharge is plotted in panel B. Here, to show overlap between the two half-cycles, the voltage-time trace during one half-cycle is vertically mirrored and shifted left, to overlap with the other voltage-time trace. In general we observe excellent agreement, and thus symmetric behavior in the two halves of the cycle, as expected. Some differences are observed between the two traces for the lower values of charge transfer, for which we do not have an explanation. Otherwise, the two voltage-time traces overlap well. Fig. 3B shows how, at the start of each half-cycle after the reversal of current direction, the cell voltage rises rapidly in time. Such a voltage spike can typically be ascribed to the effect of a linear resistance (e.g. in wires or across a separator). This effect is indeed largely responsible for the observed spike, but cannot explain it entirely, as its magnitude depends on the total charge in addition to the applied current. Thus, other aspects related to the state-of-charge of the NiHCF IHC must also have played a role.

In general, the results presented in Fig. 3 are consistent with our expectations that cell voltage gradually increases within a half-cycle, and thus for longer cycles it reaches a higher value. We also observe that – neglecting the short initial periods of negative cell voltage – in all instances the cell responds with a positive voltage when a charging current is applied (i.e., charging needs energy input). Furthermore, in none of the cycles do we see a linear increase in cell voltage versus time (or, equivalently, versus charge), as would be expected on the basis of the linear behavior of the “plateau” region of the voltage-charge curve in Fig. 2B. This deviation is linked to rate limitations mentioned before. This conclusion is by a comparison of the large cell voltages applied, to those expected based on equilibrium cycling: for a maximum charge transferred of 90 C/g-NiHCF (two electrode mass), which translates to 50 mAh/g-NiHCF (single electrode mass), each electrode will change its equilibrium potential by approximately 175 mV, and thus in the ideal case, without ion or electron transfer limitations, the potential of each electrode (i.e., with respect to a stationary reference) varies between -175 to +175 mV (neglecting the effect of concentration polarization), manifesting as a maximum cell voltage of 0.35 V. Instead, for the cycle with the highest charge, we observe the cell voltage approaching 1.0 to 1.5 V at the end of a half-cycle. Thus, we believe that transport limitations must have played a role in limiting the rate capability of the present CID experiments, as a result of sluggish pore-scale or solid-state transport processes. We reiterate that the charging behavior in 1 M Na₂SO₄ with higher current densities, as discussed in Fig. 2, did not show such strong rate limitations, but note that in such an electrolyte the Na-concentration is hundred times larger than in the CID experiments. This aspect of our electrode design requires further study and optimization.

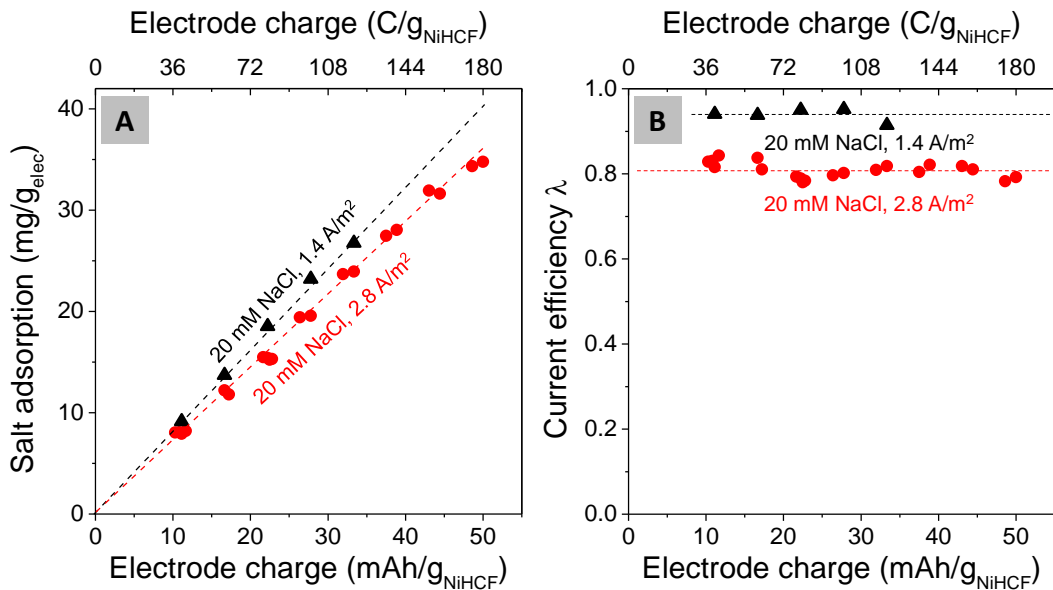


Figure 4. A) Salt adsorption capacity of NiHCF IHCs, in mg NaCl per cycle per gram of both electrodes vs. electrode charge (per gram NiHCF in one electrode) for the experiments of Fig. 3 together with data at a 2x lower current density. B) Current efficiency, which is the ratio of salt adsorption rate over current density, see Eq. (2) ($\lambda \sim 0.8$ for $I=2.8$ A/m², and $\lambda \sim 0.95$ for $I=1.4$ A/m²).

Figure 4 summarizes all data presented in Fig. 3 for a current density of 2.8 A/m² as function of electrode charge and plots salt adsorption capacity, SAC, which is expressed in mg NaCl adsorption per mass of both electrodes (not per mass of active component, which in our case is 80 wt% of the total electrode mass). The highest value of SAC here, 34 mg/g, is about 2.5 times a reference value for CDI with capacitive activated carbon electrodes of SAC=12.5 mg/g [1,34]. Though SAC in CDI can be increased to higher values when using higher cell voltages, membranes, or chemically modified electrodes [35,36], on this metric CID using NiHCF IHCs quite well competes with state-of-the-art CDI technology. Fig. 4A also presents a limited number of data at a twice lower current density (1.4 A/m²), related to one voltage-time trace that is shown in Fig. 5A. For both current densities, Fig 4B presents data for current efficiency λ , which is the ratio of average salt adsorption rate, $J_{\text{salt,avg}}$ (which is SAC multiplied by two times the electrode mass, M_{el} , divided by half-cycle time, HCT, and NaCl mass, $M_{\text{w}}=58.44$ g/mol), over current, I , in A, divided by $F=96485$ C/mol, and thus is given by

$$\lambda = (2 \cdot \text{SAC} \cdot M_{\text{el}}) / (HCT \cdot M_{\text{w}}) / (I / F) \quad (2)$$

For current efficiency, λ , both data sets show a nearly perfect independence of λ on electrode charge, with $\lambda \sim 0.8$ at 2.8 A/m² and $\lambda \sim 0.95$ at 1.4 A/m², see Fig. 4. Ideally, for perfect membranes (i.e., only counterion transport is permitted) and perfect cation intercalation, the current efficiency must be unity. Various factors may be responsible for the value of λ being less than unity. One factor contributing to this effect, at least in part, is the loss of charge through undesired side reactions, such as O₂ evolution. Such a reaction is expected to occur to a greater degree when cycling with large overpotentials that are experienced at higher current densities. Additionally, though unreported for previous PBAs using Na₂SO₄ electrolyte, it is possible that NiHCF not only intercalates Na⁺ ions, but also anions. Based on a simple model we determine that salt back-diffusion through the AEM seems an unlikely explanation under the present experimental conditions (see SI). The influence of current density on current efficiency deserves further attention and the CID process and materials should be improved to increase λ to a value much closer to unity, also at higher currents than presently employed.

Finally, we analyze the energy invested in desalination by integrating the cell voltage versus charge in one half-cycle (see Fig. 5A) and divide by salt removal (given by the salt concentration difference between inflow and outflow, multiplied by the water flow rate). Making this analysis for the data at 30 C/g-NiHCF from Fig. 3B, which results in a SAC of around 12.5 mg/g (similar to many CDI data), we obtain for 2.8 A/m² current density a value of ~ 12 kT/ion removed, and even as low as ~ 3 kT/ion at a current of 1.4 A/m² (Note that energies in kT/ion can be multiplied by 5 to obtain the energy consumption in kJ per mol salt removed), which are clearly below those for MCDI reported in refs. [1,8]. Figure 5B analyzes energy consumption in these experiments, and compares

the “energy per ion” for these two cases of CID operation, with membrane-CDI data from ref. [8]. We clearly observe that, based on this metric, CID data at the lowest current (1.4 A/m^2) show more than a five-fold reduction in energy consumption compared to MCDI. This five-fold reduction is half the factor of 10 that we calculated earlier on the basis of the difference in capacitance between capacitive and intercalation electrodes, and thus a larger gain in energy consumption is still feasible.

In conclusion, though salt adsorption rates are for now very slow, the results in Fig. 4 and 5 provide evidence that there is significant potential for an enhancement in salt adsorption capacity and a reduction in energy use in electrochemical water desalination when employing intercalation host electrodes.

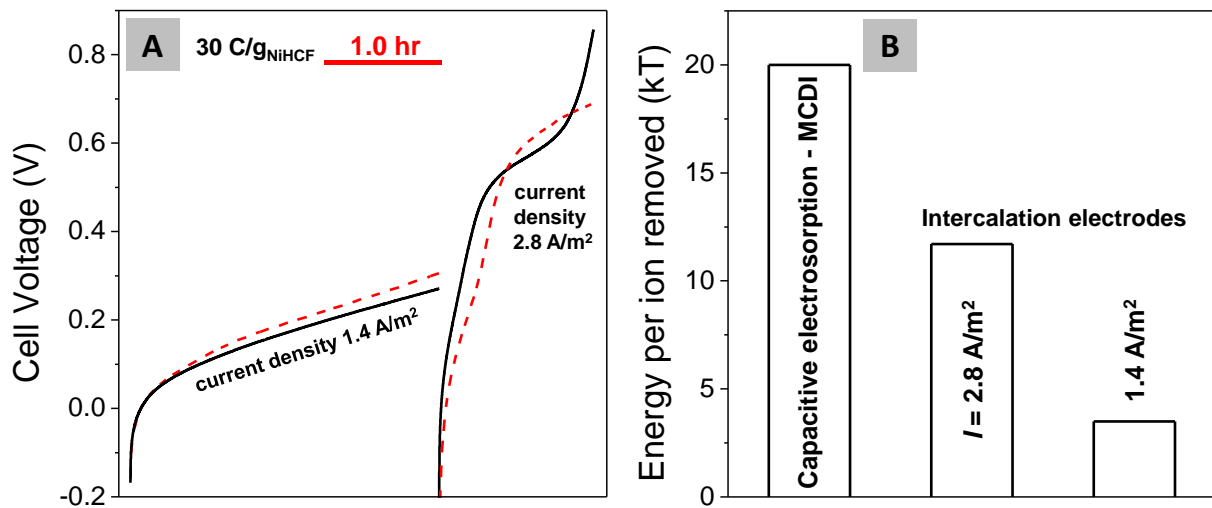


Figure 5. A) Cell voltage increase in time, for two values of the current density, in a cycle where the charge transfer is $\pm 30 \text{ C/g-NiHCF}$. B) Energy consumption per amount of salt removal, where CID cell performance with NiHCF is compared with data for membrane-CDI [8].

Methods

Synthesis. Disodium nickel hexacyanoferrate was synthesized by a solution/precipitation reaction with aqueous reagents using the following synthesis reaction: $\text{NiCl}_2 + \text{Na}_4\text{Fe}(\text{CN})_6 \rightarrow \text{Na}_2\text{NiFe}(\text{CN})_6 + 2\text{NaCl}$. A previous recipe used to synthesize Na-rich NiHCF [23] was employed with several modifications by incorporating findings from a recipe used to synthesize Na-rich manganese hexacyanoferrate [40]. In this procedure, 20 mM of $\text{Na}_4\text{Fe}(\text{CN})_6 \cdot 10\text{H}_2\text{O}$ (Sigma Aldrich) and 2.40 M of NaCl (Sigma Aldrich) were dissolved in a mixture of pure water with 25 wt% pure ethanol (compared to pure water). Subsequently, 40 mM of aqueous solution of $\text{NiCl}_2 \cdot 6\text{H}_2\text{O}$ (Alfa Aesar) was added dropwise to the mixture of $\text{Na}_4\text{Fe}(\text{CN})_6$, NaCl, water and ethanol. The solid NiHCF precipitate was filtered, washed with pure water, dried in a vacuum oven at 50°C to remove residual moisture, and ground using a ball mill.

Material Characterization. Elemental analysis was conducted with NiHCF decomposed into elemental species in acid using a PerkinElmer 2400 Series II CHN/O Elemental Analyzer and a PerkinElmer 2000DV ICP-OES instrument. X-ray diffraction was conducted using a Bruker D8 Venture instrument with Cu-K α radiation ($\lambda=1.54$ Å, 0.02° angular resolution, and $3^\circ < 2\Theta < 100^\circ$). Both samples showed slight peak broadening indicative of their nanocrystalline microstructure, and several high-angle peaks were not apparent due to background noise. Also, it should be noted that fluorescent interaction between Fe and X-Ray radiation emitted from Cu can produce mild inaccuracy in the measured intensity. N₂ adsorption measurements were performed at -196°C using a TriStar 3000 gas adsorption analyzer (Micromeritics).

SEM samples were deposited and pressed gently onto carbon tape attached to an aluminum sample holder. To minimize charging the samples were coated with approximately 4 nm of gold-palladium film using a Denton (Moorestown NJ) Desk-II turbo sputter coater, and imaged at 5 kV in HiVac mode using a Quanta 450 FEG environmental scanning electron microscope (FEI Company, Hillsboro OR). TEM samples were prepared by dispersion in deionized water by sonication in a water bath for approximately 5 minutes, followed by vibration using a Fisher S56 Minirotor touch shaker. Dried droplets were then glow-discharged on wax film and subsequently transferred to carbon-stabilized Formvar-coated TEM grids (cat. no. 01811; Ted Pella, Inc., Redding CA). TEM images were obtained using a Philips/FEI CM200 instrument at 160 and 200 kV.

Electrode Preparation. 80 wt% of the NiHCF powder was mixed with 10 wt% carbon black (Vulcan XC72R, Cabot Corp., Boston, MA) and 10 wt% polytetrafluoroethylene binder (PTFE, 60 wt% solution in water from Sigma Aldrich, USA) and pure ethanol to obtain an homogeneous slurry. The final electrodes were calendered using a rolling machine (MTI HR01, MIT Corp.) to produce a thickness of 200 μ m. Prior to CID experiments, electrodes were cut into 6x6 cm squares and dried in a vacuum oven at 50°C to remove residual moisture, which is necessary to measure electrode dry mass.

Half-Cell Characterization. Electrochemical characterization of NiHCF material was performed by constructing a three-electrode half-cell with the working electrode containing 0.98 g of NiHCF in 1 M Na₂SO₄, cycled against a titanium mesh electrode coated with Ir/Ru (Magneto Special Anodes B.V., the Netherlands) as counter electrode and Ag/AgCl as a reference electrode placed in the vicinity of the working electrode. In “bursts” of 5 C (at a current of 60 mA/g-NiHCF in the electrode) the working electrode was charged, after which a “rest period” (“OCV” for “open circuit voltage”) of 60 s follows in which the potential relaxes (see inset in Fig 2A). We continued this process until the electrode potential diverged strongly, implying full (de-)intercalation of Na ions was reached. The electrode potential at the end of each OCV period was taken as equilibrium potential (versus Ag/AgCl) and plotted as a data point in Fig 2B.

Cell Design and Testing. The experimental CID flow cell was constructed in the following way. Two end plates on the outer sides of the cell were used to sandwich meshed current collectors, NiHCF electrodes, and an AEM. In this work we used a commercial AMX Neosepta membrane with thickness of 140 μm . Meshed current collector also served as a spacer material to allow feed water to flow along the NiHCF electrode surface. The cell contained an electrode of $M_{\text{el}}=0.99$ g (of which ~ 0.8 g is NiHCF) on each side, and the membrane area available for ion transfer was 36 cm^2 . Desalination experiments were performed at a constant current of 10 mA, thus 2.77 A/m^2 , and a water flow rate of 10 mL/min directed into each channel. Constant current was applied until a certain value of charge transfer was reached (total number of Coulombs per gram of material transferred, as shown in Figs. 3 and 4). Subsequently, the current direction was reversed. After 2 or 3 similar cycles with the same total charge transfer, the charge transfer was reduced stepwise. Because all experiments in Fig. 3 were done at the same current density (which can only switch sign), the cycles become shorter in duration.

Acknowledgments

KCS acknowledges support from the Department of Mechanical Science and Engineering and the College of Engineering at the University of Illinois at Urbana-Champaign. AS acknowledges support from the Department of Materials Science and Engineering at the University of Illinois at Urbana-Champaign. Part of this work was performed in the cooperation framework of Wetsus, European Centre of Excellence for Sustainable Water Technology (www.wetsus.eu). Wetsus is co-funded by the Dutch Ministry of Economic Affairs and Ministry of Infrastructure and Environment, the Province of Fryslân, and the Northern Netherlands Provinces.

References

- [1] M.E. Suss, S. Porada, X. Sun, P.M. Biesheuvel, J. Yoon, V. Presser, Water desalination via capacitive deionization: what is it and what can we expect from it?, *Energy Environ. Sci.* 8 (2015) 2296–2319. doi:10.1039/C5EE00519A.
- [2] J. Lee, S. Kim, C. Kim, J. Yoon, Hybrid capacitive deionization to enhance the desalination performance of capacitive techniques, *Energy & Environ. Sci.* 7 (2014) 3683–3689. doi:10.1039/C4EE02378A.
- [3] M. Pasta, C.D. Wessells, Y. Cui, F. La Mantia, A Desalination Battery, *Nano Lett.* 12 (2012) 839–843. doi:10.1021/nl203889e.
- [4] K.C. Smith, R. Dmello, Na-Ion Desalination (NID) Enabled by Na-Blocking Membranes and Symmetric Na-Intercalation: Porous-Electrode Modeling, *J. Electrochem. Soc.* 163 (2016) A530–A539. doi:10.1149/2.0761603jes.
- [5] P. Srimuk, F. Kaasik, B. Krüner, A. Tolosa, S. Fleischmann, N. Jäckel, M.C. Tekeli, M. Aslan, M.E. Suss, V. Presser, MXene as a novel intercalation-type pseudocapacitive cathode and anode for capacitive deionization, *J. Mater. Chem. A* 4 (2016) 18265–18271. doi:10.1039/C6TA07833H.
- [6] F. Xing, T. Li, J. Li, H. Zhu, N. Wang, X. Cao, Chemically exfoliated MoS₂ for capacitive deionization of saline water, *Nano Energy* 31 (2017) 590–595. doi:10.1016/j.nanoen.2016.12.012.
- [7] G.J. Doornbusch, J.E. Dykstra, P.M. Biesheuvel, M.E. Suss, Fluidized bed electrodes with high carbon

loading for water desalination by capacitive deionization, *J. Mater. Chem. A*. 4 (2016) 3642–3647. doi:10.1039/C5TA10316A.

[8] J.E. Dykstra, R. Zhao, P.M. Biesheuvel, A. van der Wal, Resistance identification and rational process design in Capacitive Deionization, *Water Res.* 88 (2016) 358–370. doi:10.1016/j.watres.2015.10.006.

[9] Y. Qu, P.G. Campbell, L. Gu, J.M. Knipe, E. Dzenitis, J.G. Santiago, M. Stadermann, Energy consumption analysis of constant voltage and constant current operations in capacitive deionization, *Desalination*. 400 (2016) 18–24. doi:10.1016/j.desal.2016.09.014.

[10] T. Kim, J.E. Dykstra, S. Porada, A. van der Wal, J. Yoon, P.M. Biesheuvel, Enhanced charge efficiency and reduced energy use in capacitive deionization by increasing the discharge voltage, *J. Colloid Interface Sci.* 446 (2015) 317–326. doi:10.1016/j.jcis.2014.08.041.

[11] C. Prehal, D. Weingarth, E. Perre, R.T. Lechner, H. Amenitsch, O. Paris, V. Presser, Tracking the structural arrangement of ions in carbon supercapacitor nanopores using *in situ* small-angle X-ray scattering, *Energy Environ. Sci.* 8 (2015) 1725–1735. doi:10.1039/C5EE00488H.

[12] S. Kim, J. Lee, C. Kim, J. Yoon, $\text{Na}_2\text{FeP}_2\text{O}_7$ as a Novel Material for Hybrid Capacitive Deionization, *Electrochim. Acta*. 203 (2016) 265–271. doi:10.1016/j.electacta.2016.04.056.

[13] K.C. Smith, R. Dmello, Desalination Devices, 62/427,502, 2016.

[14] H. Kim, J. Hong, K.-Y. Park, H. Kim, S.-W. Kim, K. Kang, Aqueous Rechargeable Li and Na Ion Batteries, *Chem. Rev.* 114 (2014) 11788–11827. doi:10.1021/cr500232y.

[15] J.F. Whitacre, A. Tevar, S. Sharma, $\text{Na}_4\text{Mn}_9\text{O}_{18}$ as a positive electrode material for an aqueous electrolyte sodium-ion energy storage device, *Electrochem. Commun.* 12 (2010) 463–466. doi:10.1016/j.elecom.2010.01.020.

[16] Z. Li, D. Young, K. Xiang, W.C. Carter, Y.-M. Chiang, Towards High Power High Energy Aqueous Sodium-Ion Batteries: The $\text{NaTi}_2(\text{PO}_4)_3/\text{Na}_0.44\text{Mn}_2\text{O}_3$ System, *Adv. Energy Mater.* 3 (2013) 290–294. doi:10.1002/aenm.201200598.

[17] J.F. Whitacre, S. Shanbhag, A. Mohamed, A. Polonsky, K. Carlisle, J. Gulakowski, W. Wu, C. Smith, L. Cooney, D. Blackwood, J.C. Dandrea, C. Truchot, A Polyionic, Large-Format Energy Storage Device Using an Aqueous Electrolyte and Thick-Format Composite $\text{NaTi}_2(\text{PO}_4)_3/\text{Activated Carbon}$ Negative Electrodes, *Energy Technol.* 3 (2015) 20–31. doi:10.1002/ente.201402127.

[18] Z. Li, D.B. Ravnsbæk, K. Xiang, Y.-M. Chiang, $\text{Na}_3\text{Ti}_2(\text{PO}_4)_3$ as a sodium-bearing anode for rechargeable aqueous sodium-ion batteries, *Electrochem. Commun.* 44 (2014) 12–15. doi:10.1016/j.elecom.2014.04.003.

[19] X. Wu, Y. Cao, X. Ai, J. Qian, H. Yang, A low-cost and environmentally benign aqueous rechargeable sodium-ion battery based on $\text{NaTi}_2(\text{PO}_4)_3-\text{Na}_2\text{NiFe}(\text{CN})_6$ intercalation chemistry, *Electrochem. Commun.* 31 (2013) 145–148. doi:10.1016/j.elecom.2013.03.013.

[20] C.D. Wessells, S. V. Peddada, R.A. Huggins, Y. Cui, Nickel hexacyanoferrate nanoparticle electrodes for aqueous sodium and potassium ion batteries, *Nano Lett.* 11 (2011) 5421–5425. doi:10.1021/nl203193q.

[21] C.D. Wessells, R.A. Huggins, Y. Cui, Copper hexacyanoferrate battery electrodes with long cycle life and high power, *Nat. Commun.* 2 (2011) 550.

[22] X. Wu, M. Sun, Y. Shen, J. Qian, Y. Cao, X. Ai, H. Yang, Energetic Aqueous Rechargeable Sodium-Ion Battery Based on $\text{Na}_2\text{CuFe}(\text{CN})_6-\text{NaTi}_2(\text{PO}_4)_3$ Intercalation Chemistry, *ChemSusChem.* 7 (2014) 407–411.

[23] X. Wu, Y. Cao, X. Ai, J. Qian, H. Yang, A low-cost and environmentally benign aqueous rechargeable sodium-ion battery based on $\text{NaTi}_2(\text{PO}_4)_3-\text{Na}_2\text{NiFe}(\text{CN})_6$ intercalation chemistry, *Electrochem. Commun.* 31 (2013) 145–148. doi:10.1016/j.elecom.2013.03.013.

[24] R.Y. Wang, C.D. Wessells, R.A. Huggins, Y. Cui, Highly reversible open framework nanoscale electrodes for divalent ion batteries, *Nano Lett.* 13 (2013) 5748–5752. doi:10.1021/nl403669a.

[25] A.L. Lipson, B. Pan, S.H. Lapidus, C. Liao, J.T. Vaughey, B.J. Ingram, Rechargeable Ca-Ion Batteries: A New Energy Storage System, *Chem. Mater.* 27 (2015) 8442–8447. doi:10.1021/acs.chemmater.5b04027.

[26] L. Zhang, L. Chen, X. Zhou, Z. Liu, Morphology-Dependent Electrochemical Performance of Zinc

Hexacyanoferrate Cathode for Zinc-Ion Battery, *Sci. Rep.* 5 (2015) 18263. doi:10.1038/srep18263.

[27] K.C. Smith, Theoretical evaluation of electrochemical-cell architectures using cation intercalation electrodes for desalination, Submitted. (2016).

[28] H.J. Buser, D. Schwarzenbach, W. Petter, A. Ludi, The crystal structure of Prussian Blue: $\text{Fe}_4[\text{Fe}(\text{CN})_6]_3 \cdot x\text{H}_2\text{O}$, *Inorg. Chem.* 16 (1977) 2704–2710. doi:10.1021/ic50177a008.

[29] Y. Yue, Z. Zhang, A.J. Binder, J. Chen, X. Jin, S.H. Overbury, S. Dai, Hierarchically superstructured Prussian blue analogues: Spontaneous assembly synthesis and applications as pseudocapacitive materials, *ChemSusChem.* 8 (2015) 177–183. doi:10.1002/cssc.201402520.

[30] J. Jagiello, J.P. Olivier, 2D-NLDFT adsorption models for carbon slit-shaped pores with surface energetical heterogeneity and geometrical corrugation, *Carbon N. Y.* 55 (2013) 70–80. doi:10.1016/j.carbon.2012.12.011.

[31] S. Porada, F. Schipper, M. Aslan, M. Antonietti, V. Presser, T.P. Fellinger, Capacitive Deionization using Biomass-based Microporous Salt-Templated Heteroatom-Doped Carbons, *ChemSusChem.* 8 (2015) 1823. doi:10.1002/cssc.201500696.

[32] K.C. Smith, R. Dmello, Comment on: “Na-Ion Desalination (NID) Enabled by Na-Blocking Membranes and Symmetric Na-Intercalation: Porous-Electrode Modeling” [*J. Electrochem. Soc.*, 163, A530 (2016)], *J. Electrochem. Soc.* 163 (2016) Y17–Y17. doi:10.1149/2.0601610jes.

[33] B. Scroscatti, Lithium Rocking Chair Batteries: An Old Concept?, *J. Electrochem. Soc.* 139 (1995) 2776–2781.

[34] S. Porada, P.M. Biesheuvel, V. Presser, Comment on Sponge-Templated Preparation of High Surface Area Graphene with Ultrahigh Capacitive Deionization Performance, *Adv. Funct. Mater.* 25 (2015) 179–181. doi:10.1002/adfm.201401101.

[35] P.M. Biesheuvel, H.V.M. Hamelers, M.E. Suss, Theory of Water Desalination by Porous Electrodes with Immobile Chemical Charge, *Colloids Interface Sci. Comm.* 9 (2016) 1–5. doi:10.1016/j.colcom.2015.12.001.

[36] X. Gao, S. Porada, A. Omosebi, K. Liu, P.M. Biesheuvel, J. Landon, Complementary surface charge for enhanced capacitive deionization, *Water Res.* 92 (2016) 275–282. doi:10.1016/j.watres.2016.01.048.

[37] B.E. Conway, Electrochemical Supercapacitors: Scientific Fundamentals and Technological Applications, 1991. doi:10.1017/CBO9781107415324.004.

[38] K.C. Smith, Simulation of Na-Ion Intercalation Electrodialysis Using Prussian-Blue Analogues, Submitted. (2016).

[39] K.C. Smith, Theoretical evaluation of electrochemical cell architectures using cation intercalation electrodes for desalination, Submitted. (2016).

[40] J. Song, L. Wang, Y. Lu, J. Liu, B. Guo, P. Xiao, J.J. Lee, X.Q. Yang, G. Henkelman, J.B. Goodenough, Removal of interstitial H_{2}O in hexacyanometallates for a superior cathode of a sodium-ion battery, *J. Am. Chem. Soc.* 137 (2015) 2658–2664. doi:10.1021/ja512383b.